Journal of Alloys and Compounds 509 (2011) 9536–9541

Contents lists available at ScienceDirect

Journal of Alloys and Compounds

journal homepage: www.elsevier.com/locate/jallcom

Effect of annealing on pulsed laser deposited zirconium oxide thin films

M.F. Al-Kuhaili*, S.M.A. Durrani

Physics Department, King Fahd University of Petroleum and Minerals, Dhahran 31261, Saudi Arabia

ARTICLE INFO

Article history:
Received 17 June 2011
Received in revised form 19 July 2011
Accepted 21 July 2011
Available online 27 July 2011

Keywords:
Zirconium oxide
Pulsed laser deposition
Annealing

ABSTRACT

Zirconium oxide thin films were deposited using pulsed laser ablation from a ceramic ZrO_2 target on unheated substrates. Subsequently, the films were annealed in air in the temperature range 400–800 °C. The films were characterized by X-ray diffraction, atomic force microscopy, X-ray photoelectron spectroscopy, and optical spectroscopy to investigate the variation of the structural, chemical, and optical properties upon annealing. As-deposited films were amorphous and had a large surface density of ablated particles. Annealing resulted in the growth of monoclinic nano-crystalline, uniform, and transparent films that were slightly sub-stoichiometric. The annealed films were compact and had high values of the refractive index. Extinction coefficients were small, and may be related to the presence of defects. The films exhibited the presence of an indirect band gap, related to defects, and a direct band gap, related to fundamental absorption.

1. Introduction

Zirconium oxide (ZrO_2) is a material that has found numerous applications in diverse technological fields due to a unique combination of attractive properties. It possesses a high thermal expansion coefficient and a high melting point [1,2]. It is also characterized by mechanical strength, low thermal conductivity, excellent thermal stability, large resistance against oxidation, chemical durability, and fracture toughness [1–3]. Thus, it has found important applications in protective coatings, such as thermal barrier coatings [1,4]. From an optical point of view, ZrO_2 has a wide band gap, high refractive index, large transparency in the visible and infrared ranges, and high laser damage threshold [1–3]. Because of these excellent optical properties, ZrO_2 has been widely used in various optical applications, including high reflectivity mirrors, broadband interference filters, and low-loss waveguides [1–5]. In addition, zirconium oxide has a large dielectric constant [4]. Thus, it has emerged as a promising candidate to replace SiO_2 as the gate dielectric in complementary metal oxide semiconductor technology [2].

Zirconium oxide thin films have been prepared by a variety of techniques including ion-beam assisted deposition [1], sputtering [2,3,5], cathodic arc deposition [4,6,7], sol–gel [8–11], atomic layer deposition [12], and thermal oxidation of zirconium [13]. ZrO_2 thin films have been fabricated by pulsed laser deposition (PLD) mostly using the ultraviolet krypton fluoride (KrF) excimer laser. The films were prepared by reactive laser ablation of a pure zirconium target in an oxygen atmosphere [14,15]. Alternatively, ZrO_2 thin films were prepared by PLD using a ZrO_2 ceramic target [16–20]. Post-deposition annealing of thin films leads to densification and higher packing density [21]. Moreover, annealing results in the enhancement of crystallization and thus reduction of structural defects. Both effects (densification and crystallization) are important from an application viewpoint. There is only a single study on the post-deposition annealing of ultrathin (~12 nm) ZrO_2 thin films prepared by PLD and subsequently annealed at 400 °C.

In this work, zirconium oxide thin films were prepared by pulsed laser deposition, and were subsequently annealed in air in the temperature range 400–800 °C. The effect of annealing on the structural, chemical and optical properties of the films was investigated.

2. Experiment

Zirconium oxide thin films were prepared by pulsed laser deposition using ZrO_2 targets (K.J. Lesker with a purity of 99.9%). A KrF pulsed excimer laser (Lambda Physik Compex Pro 102), with a wavelength of 248 nm, was used to ablate the targets. The laser provided pulses with pulse duration of 12–16 ns at a repetition rate of 10 Hz. The energy per pulse was 300 mJ. The angle between the incident laser beam and the normal to the target surface was 45°. In each deposition, 10,000 laser pulses were used. In order to obtain uniform films and to avoid depleting the target material at the same spot, the target and the substrates were rotated at a speed of 100 rpm during the laser irradiation. The target-to-substrate distance was 5.5 cm. The films were simultaneously deposited on unheated fused silica substrates (for optical and structural characterization) and tantalum substrates (for chemical analysis). The base pressure of the deposition chamber was 2×10^{-3} Pa. The

* Corresponding author. Tel.: +966 3 860 3747; fax: +966 3 860 2293.
E-mail address: kuhaili@kfupm.edu.sa (M.F. Al-Kuhaili).

0925-8388/$ – see front matter © 2011 Elsevier B.V. All rights reserved.
doi:10.1016/j.jallcom.2011.07.062

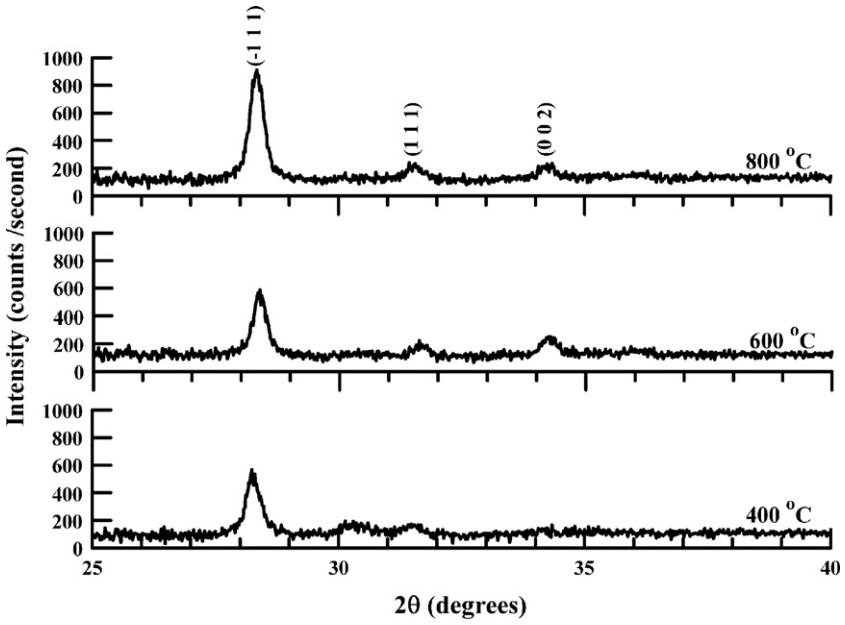

Fig. 1. XRD patterns of the annealed films. The annealing temperature is indicated on each spectrum.

as-deposited films were post-annealed in air at temperatures (T_a) of 400, 600, and 800 °C for 4 h in each annealing. After annealing, the films were allowed to cool back to room temperature while still in the oven for 6 h.

The thickness of the as-deposited films was measured using a stylus surface profilometer (Ambiox XP-2), and was found to be 165 ± 5 nm. The structure of the films was investigated by X-ray diffraction (XRD) using a Shimadzu XRD-6000 diffractometer, employing Cu Kα radiation. The 2θ step and step acquisition time were 0.02° and 1.00 s, respectively. The surface morphology of the films was examined by contact mode atomic force microscopy (AFM) (Veeco Innova diSPM). The sample surface was probed with a silicon tip of 10 nm radius oscillating at its resonant frequency of 300 kHz. The scan area was $2 \times 2\ \mu m^2$, and the scan rate was 2 Hz. The chemical composition of the films was studied using X-ray photoelectron spectroscopy (XPS), and was performed in a VG Scientific ESCALAB MKII spectrometer equipped with an Al Kα (1486.6 eV) X-ray source. The instrumental resolution was 1.2 eV, with a slit width of 0.6 cm. Prior to the XPS analysis, the samples were transferred in air to the XPS analysis chamber. The C 1s peak of hydrocarbon contamination, at a binding energy of 284.5 eV, was used as the binding energy reference. During the XPS analysis, the samples were maintained at ambient temperature at a pressure of 5×10^{-7} Pa. The optical properties of the films were determined by measuring normal-incidence transmittance (T) of the films, over the wavelength range 200–1200 nm, using a Jasco V-570 double beam spectrophotometer.

3. Results and analysis

3.1. Structural and morphological properties

Zirconium oxide is a material that exhibits three polymorphs: monoclinic, tetragonal and cubic. The monoclinic phase is found up to 1170 °C, the tetragonal phase is observed between 1170 and 2370 °C, and the cubic phase is observed up to the melting point 2680 °C [2,9]. Thus, at low temperatures (<1000 °C), the equilibrium phase is the monoclinic. However, under some special conditions, such as those that exist during film deposition, polymorphs can exist at much lower temperatures [22]. The crystalline phase that results depends on the deposition technique and the annealing temperature. For example, ZrO_2 thin films deposited by sol–gel are usually amorphous. They have a tetragonal structure when annealed at 400–500 °C, and a monoclinic phase when annealed at temperatures higher than 700 °C [9,23]. On the other hand, films deposited by DC reactive sputtering [2] or filtered cathodic vacuum arc [7] had a monoclinic structure.

In this work, the as-deposited films were amorphous. This was attributed to the high heat of formation of ZrO_2, which hinders the re-arrangement of oxygen–metal bonds at low temperatures, and thus the formation of a crystalline phase [2]. It was pointed out that ablated species can have kinetic energies that range from 0.01 eV to several hundred electron volts [24]. Such energetic particles can easily penetrate the growing film and create defects in the film [24]. Thus, PLD films deposited in vacuum tend to be amorphous [25].

The annealed films grew in a monoclinic phase, as revealed by the XRD spectra shown in Fig. 1. The phase identification was based on comparison with data from the JCPDS international diffraction database. The intensity of the XRD spectra increased with the annealing temperature. Annealing induces coalescence between crystals and results in an enhanced crystalline growth [11]. The dominance of the monoclinic phase can be understood on the basis of the thermodynamics of crystal growth. Generally, the crystal plane with the lowest Gibbs free energy will grow preferentially [7]. In ZrO_2, this plane corresponds to the monoclinic ($\bar{1}$ 1 1) orientation [7].

The average crystallite size (L) was estimated from the ($\bar{1}$ 1 1) diffraction peak using the Scherrer formula [9]:

$$L = \frac{0.89\lambda_\alpha}{G\cos\theta} \quad (1)$$

where λ_α is the wavelength of the Cu Kα radiation (1.54 Å), G is the full width at half maximum of the ($\bar{1}$ 1 1) peak, and θ is the diffraction angle corresponding to that peak. The calculated average crystallite sizes are given in Table 1. From these values, it can be concluded that the annealed films had a nano-crystalline structure. The crystallite size of the films annealed at 800 °C was less than that of the films annealed at 600 °C. A similar effect was observed in sol–gel deposited ZrO_2 thin films, and was attributed to the onset of monoclinic → tetragonal transformation, which takes place in the annealing temperature range of 850–950 °C [23]. Despite the

Table 1
Summary of the structural properties of the films.

T_a (°C)	L (nm)	R_{rms} (nm)
400	23.1	2.84
600	25.3	8.76
800	23.8	3.98

T_a: annealing temperature, L: crystallite size, R_{rms}: root-mean-square roughness.

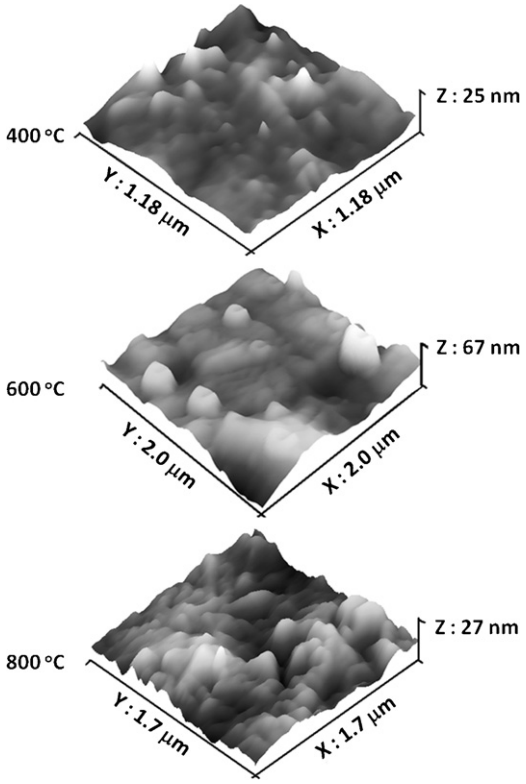

Fig. 2. Three-dimensional AFM micrographs of the annealed films.

decrease in crystallite size of the films annealed at 800 °C, these films had the highest XRD peak intensity. This increase in the XRD peak intensity is not due to the crystallite size but rather to an increase in the number of crystallites [10].

The surfaces of the as-deposited films were covered with particulates that were ejected from the target during the ablation process. Annealing provided these particulates with sufficient thermal energy to re-evaporate or diffuse laterally on the substrate surface. This suggests that the particulates were loosely bound to the substrate surface. Thus, annealing resulted in the evolution of smooth and homogeneous surfaces that were free of any particles. The effect of annealing on the surface morphology was investigated by AFM. Typical three-dimensional AFM micrographs are shown in Fig. 2. On the nano-scale, the annealed films had non-uniform and rough surfaces. The root-mean-square roughness (R_{rms}) of the films is given in Table 1. The surface roughness is attributed to grain growth [7] and followed the same trend as the crystallite size.

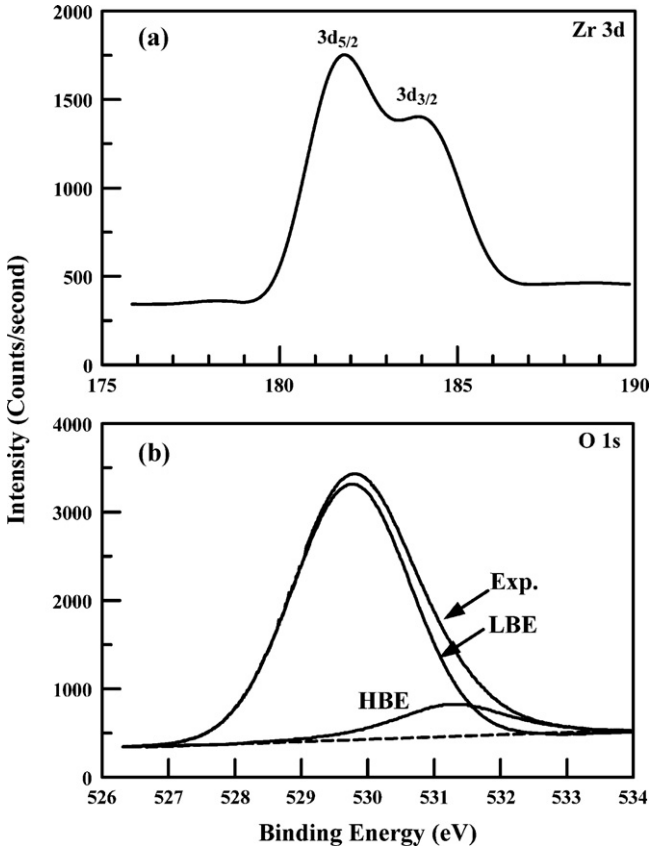

Fig. 3. Typical XPS core level spectra of an annealed film: (a) in the Zr 3d region, showing the spin–orbit split levels ($3d_{5/2}$ and $3d_{3/2}$); and (b) in the O 1s region, showing resolution of the spectrum into a low binding energy component (LBE) and a high binding energy component (HBE), the Shirley background is shown by the dashed line.

3.2. Chemical properties

The chemical state of the films was investigated using XPS. This technique is sensitive to core level shifts and can give information on the metal environment and oxidation state [8]. XPS spectra were obtained in the Zr 3d and O 1s core level regions, and are shown in Fig. 3. No significant changes in the chemical states of the films were observed as the annealing temperature was increased from 400 to 800 °C. The Zr 3d spectrum consists of two peaks ($3d_{3/2}$ and $3d_{5/2}$) that are due to spin–orbit splitting. In order to resolve these peaks, the Zr 3d spectrum was de-convoluted into two components using a Gaussian–Lorenzian mixed function employing Shirley background correction. The binding energies (BE) obtained from this analysis are given in Table 2. Similarly, the O 1s peak was resolved into two components: a low binding energy component (LBE) and a high binding energy component (HBE). The results of this decomposition

Table 2
Summary of the chemical properties of the films.

Film type	Zr 3d			O 1s			Δ (eV)
	Zr $3d_{5/2}$ BE (eV)	Zr $3d_{3/2}$ BE (eV)	δ (eV)	LBE (eV)	HBE (eV)	R	
As-deposited	182.3	184.7	2.4	530.2	531.6	0.25	347.9
Annealed	181.7	184.0	2.3	529.8	531.3	0.11	348.1

BE: binding energy, δ: difference in BE between Zr $3d_{5/2}$ and Zr $3d_{3/2}$, LBE: low BE component, HBE: high BE component, Δ: BE difference between the Zr $3d_{5/2}$ and O 1s LBE levels.

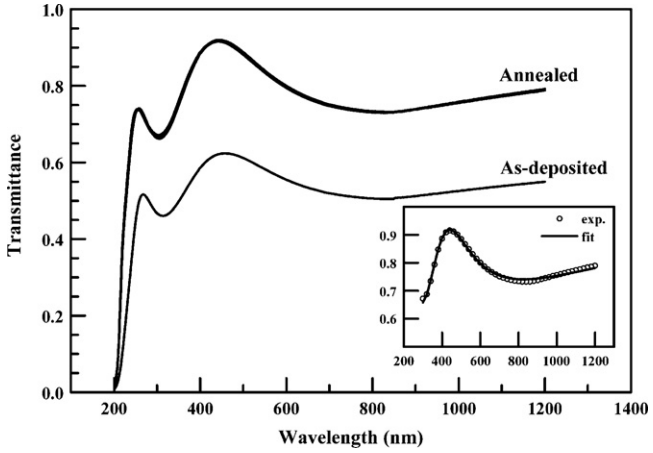

Fig. 4. Transmittance spectra of the films. The inset shows theoretical fitting of the experimental transmittance using the model presented in the text.

are also given in Table 2. Our values of the spin–orbit split of the Zr 3d level (δ) and the binding energy difference (Δ) between the Zr $3d_{5/2}$ and O 1s LBE component are in close agreement with the reported values of δ = 2.37–2.39 eV [23], and Δ = 348.3 eV [13].

The oxidation state of zirconium can be inferred from the binding energy of the Zr $3d_{5/2}$ peak. The binding energies of Zr $3d_{5/2}$ in ZrO_2 (oxidation state Zr^{4+}) were reported to be in the range 182.2–182.6 eV [4,8,23]. Thus, our as-deposited films can be assigned as stoichiometric ZrO_2. As the oxidation state of zirconium is lowered, the binding energy of Zr $3d_{5/2}$ is shifted to lower values [1,23]. Thus, the annealed films in our work were sub-stoichiometric. The down-shift of binding energy was reported to be 1.06 eV per oxidation state with respect to the Zr^{4+} [23]. Matsuoka et al. [1] reported the down-shit to be 1.03 eV per oxidation state. Using these values of down-shift and the binding energy values given in Table 2, it is estimated that the oxidation state of the annealed films was in the range 3.43–3.50, and thus the chemical state of the annealed films may be written as $ZrO_{1.73}$.

In the O 1s region, the LBE component is attributed to oxygen in zirconium oxide (Zr^{4+}). Reported values for the binding energy of the LBE component were in the range 529.5–530.2 eV [6,18,23,26]. The HBE component may correspond to oxygen in the form of a hydroxide or other adsorbed species [6]. Binding energies for the HBE component were reported in the range 531.0–532.1 eV [6,23,26]. The ratio (R) of the HBE component to the total O 1s peak, as calculated from the areas under the peak, is given in Table 2, which indicates that the HBE component was significantly reduced upon annealing.

3.3. Optical constants

The transmittance spectra of the films are shown in Fig. 4. Annealing resulted in a significant enhancement of transmittance. The annealed films were transparent down to a wavelength of 250 nm. There was a slight variation (<2%) in the transmittance of the annealed films as a function of annealing temperature. The surfaces of the as-deposited films had a large density of ablated particles. Therefore, the optical constants of such films were mainly affected by morphological features rather than material properties. Thus, the optical constants are reported only for annealed films, characterized by homogeneous surfaces that were free of particles, and which had high transparency.

In the visible and near-infrared wavelength ranges, the transmittance spectra were fitted using the equation for the transmittance of a thin film on a transparent substrate [27,28]:

$$T = \frac{16 n_s (n^2 + k^2)\beta}{A + B\beta^2 + 2\beta[C\ \cos(4\pi nd/\lambda) + D\sin(4\pi nd/\lambda)]} \quad (2)$$

with

$$A = [(n+1)^2 + k^2][(n+n_s) + k^2]$$
$$B = [(n-1)^2 + k^2][(n-n_s) + k^2]$$
$$C = -(n^2 - 1 + k^2)(n^2 - n_s^2 + k^2) + 4k^2 n_s$$
$$D = 2kn_s(n^2 - 1 + k^2) + 2k(n^2 - n_s^2 + k^2)$$

where n is the refractive index of the film, k is the extinction coefficient of the film, n_s is the refractive index of the substrate, d is the thickness of the film, λ is the wavelength of light, and $\beta = \exp(-4\pi kd/\lambda)$. In order to fit the experimental transmittance spectra using Eq. (2), models for the dispersion of n and k must be implemented.

The refractive index of the films was modeled by a single oscillator model [29]:

$$n = \left(1 + \frac{E_o E_d}{E_o^2 - E^2}\right)^{1/2} \quad (3)$$

where E_o is the effective oscillator energy, E_d is the dispersion energy related to the interband transition strength, and E is the incident photon energy ($E = hc/\lambda$, where h is Planck's constant, and c is the speed of light in vacuum). The oscillator energy (E_o) is typically near the main peak of the imaginary part of the dielectric function [5]. The dispersion energy (E_d) is directly related to the structural order of the films, where it increases with enhanced crystallinity [5].

The extinction coefficient of the films was modeled by an equation that takes into account the major absorption mechanisms in this spectral region: the Urbach tail, defect absorption, multiphoton absorption, and light scattering [30]. The λ-dependence of these processes is complicated, but if the total absorption coefficient due to these processes is small, k can be expressed as:

$$k(\lambda) = a_o + \frac{a_1}{\lambda} \quad (4)$$

where a_o and a_1 are constants.

The experimental transmittance spectra were fitted using Eq. (2), with Eqs. (3) and (4) as models for the optical constants. The fitting parameters were E_o, E_d, a_o, a_1, and d. The substrate refractive index was taken from Ref. [31]. The calculated transmittance spectra, employing the above models for n and k successfully fitted the measured spectra throughout the visible and near-infrared wavelength ranges with a correlation that was better than 99%, as shown in the inset of Fig. 4. The best-fit parameters are shown in Table 3, and they were used to calculate the optical constants of the films, which are shown by the dispersion curves of Fig. 5 (for n) and Fig. 6 (for k).

Table 3
Summary of the optical properties.

Annealing temperature	E_o (eV)	E_d (eV)	E_{gi} (eV)	E_{gd} (eV)	a_o	a_1 (nm)	d (nm)
400 °C	8.56	27.9	5.17	5.75	0.0045	3.97	101
600 °C	9.62	31.5	5.30	5.76	0.0044	4.64	101
800 °C	9.69	32.2	5.28	5.75	0	6.53	100

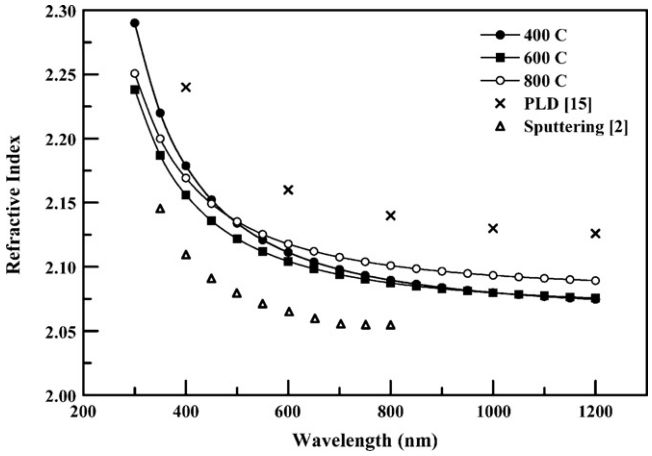

Fig. 5. Dispersion curves of the refractive index as a function of the annealing temperature. Some of the values reported in the literature are also included for comparison.

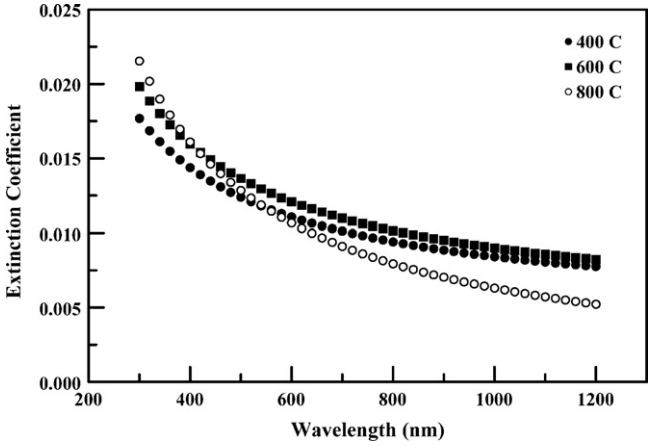

Fig. 6. Extinction coefficient as a function of wavelength for different annealing temperatures.

The refractive index showed insignificant variation with the annealing temperature. Our values of the refractive index are compared with some of the reported values in Fig. 5. There is a wide scatter in the reported values of the refractive index of ZrO_2 thin films. Values as low as 1.91 [12] and as large as 2.22 [6] were reported for the refractive index of ZrO_2 thin films at $\lambda = 550$ nm. Moreover, some studies showed that the refractive index decreased upon annealing [9,32], whereas others showed an increase of the refractive index upon annealing [5,12]. This wide variation reflects the critical dependence of the optical constants on the deposition technique, thickness, treatment (plasma or bias), annealing temperature and atmosphere, and the analytical technique (ellipsometry or spectrophotometry) used to derive the optical constants. Many studies indicated that the extinction coefficient (k) of zirconium oxide was almost zero in the visible and infrared ranges [2,15]. In our work, we found small values of k, indicating absorption that may be attributed to surface roughness and sub-stoichiometry.

The refractive index is related to the density of the films, which may be estimated from the Lorentz–Lorenz relation [33]:

$$\frac{\rho_f}{\rho_b} = \frac{(n_f^2 - 1)(n_b^2 + 2)}{(n_f^2 + 2)(n_b^2 - 1)} \quad (5)$$

where ρ_f is the density of the film, ρ_b is the density of the bulk material, n_f is the film's refractive index (Fig. 5), and n_b is the bulk refractive index whose value is 2.148 at $\lambda = 633$ nm [34]. Using n_f values of 2.121 (400 °C), 2.112 (600 °C) and 2.125 (800 °C), the density of the films were 0.98–0.99 of the bulk value; indicating the compact and dense nature of the films. Such compactness is a necessary requirement for optical applications.

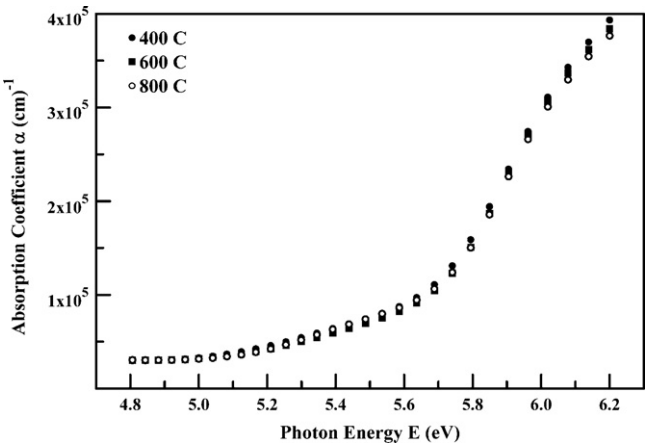

Fig. 7. The absorption coefficient as a function of incident photon energy for different annealing temperatures.

3.4. Energy band gap

In the fundamental absorption region, the absorption coefficient (α) is related to the transmittance by: $T = e^{-\alpha d}$, from which, $\alpha = (1/d) \times \ln(1/T)$. The absorption coefficient was calculated using the above equation, and the results are shown in Fig. 7. The absorption coefficient of the films showed a monotonic increase with photon energy. Similar to the behavior of the refractive index, the absorption coefficient did not change significantly with the annealing temperature. Close to the absorption edge of a semiconductor material, the energy-dependence of the absorption coefficient is given by [35]:

$$\alpha = \frac{\alpha_o}{E}(E - E_g)^{\eta} \quad (6)$$

where α_o is a constant with values between 10^5–10^6 cm^{-1} [35], and E_g is the band gap of the semiconductor. The constant η depends on the type of transitions involved: $\eta = 1/2$ corresponds to a direct transition, and $\eta = 2$ corresponds to an indirect transition. The absorption coefficient (calculated from the transmittance and shown in Fig. 7) was fitted using Eq. (6). Both direct and indirect transitions were investigated. The resulting band gap values are shown in Table 3, where E_{gi} denotes an indirect band gap and E_{gd} denotes a direct band gap. An example of the fit to direct and indirect band gaps is shown in Fig. 8. The indirect band gaps varied slightly with the annealing temperature, whereas the direct band gaps did not show any significant variation.

Zirconium oxide possesses both a direct and an indirect band gaps. There is a discrepancy about the nature of the band gap of ZrO_2. Based on band structure calculations, Kralik et al. [36], showed that ZrO_2 has a fundamental indirect band gap that corresponds to an $X \rightarrow \Gamma$ transition. On the other hand, French et al. [37] and Chang et al. [11] asserted that ZrO_2 has a direct band gap. According to Chang et al. [11], the formation of indirect transitions could be due to the existence of defects that introduce alternative energy levels between the intrinsic bands, and consequently reduce the band gap. In the monoclinic phase, the indirect band gap results from defects originating primarily from oxygen vacancies [11]. Indeed, our XPS results indicated that the annealed films were slightly sub-stoichiometric, and thus were oxygen-deficient.

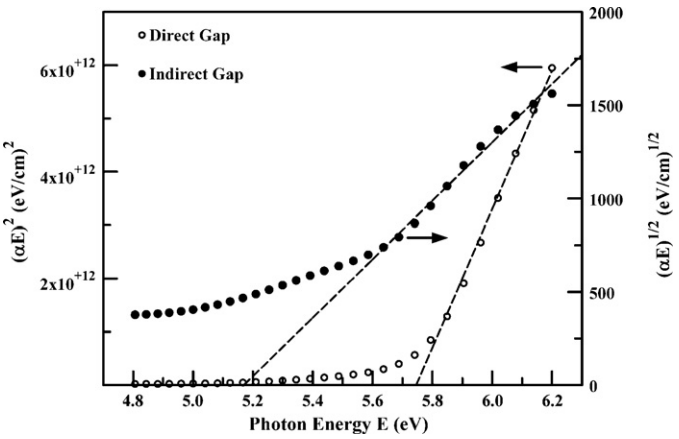

Fig. 8. $(\alpha E)^2$ [direct energy gap] and $(\alpha E)^{1/2}$ [indirect energy gap] as functions of incident photon energy for films annealed at 400 °C. The respective band gaps are given by the horizontal intercepts.

Theoretically, the indirect band gap was reported to be in the range 3.12–5.42 eV [36], whereas the direct band gap was reported to be 4.46 eV [37]. Experimentally, the indirect band gap was reported to be in the range 4.52–5.4 eV [2,7,10,11,38], whereas the direct band gap was reported to be in the range 5.65–6.01 eV [5,11,37]. The theoretical calculations underestimate the band gaps [37]. This is attributed to different parameters being taken into account for modeling [11]. In addition to the deposition technique, the reported values of the experimental band gap were sensitive to the oxygen partial pressure [2], substrate temperature [7], and annealing temperature [11,32]. The nature adopted for the band gap (direct vs. indirect) will correspondingly dictate the value of the band gap. Moreover, the experimental measurement technique can have an effect on the value of the band gap. For example, French et al. [37] reported that the band gaps determined from reflectance experiments were higher than those determined from transmittance measurements. Our values of the indirect band gap (5.25 ± 0.08 eV) were in close agreement to the value of 5.3 eV reported for sputtered ZrO_2 thin films [39]. Similarly, our values of the direct band gap (5.75 ± 0.01 eV) were in close agreement to the values of 5.65–5.74 eV reported for sputtered ZrO_2 thin films [5], and 5.78–6.01 reported for sol–gel deposited ZrO_2 thin films [11].

4. Conclusions

Zirconium oxide thin films were prepared by pulsed laser deposition on unheated substrates. The as-deposited films were amorphous and stoichiometric, but with a large surface density of ablated particles. They were also characterized by poor transparency. In order to improve the properties of the films, they were annealed in air at temperatures of 400, 600, and 800 °C. Upon annealing, the films were transformed into a polycrystalline structure with a monoclinic phase. The crystallite size was 23–26 nm. The surfaces of the annealed films were smooth and homogeneous, with a root-mean-square roughness in the range 3–9 nm. On the contrary, the films became sub-stoichiometric after annealing with a composition of $ZrO_{1.73}$. The refractive index had a value of 2.12 at 550 nm, which was close to the bulk value. The films exhibited two band gaps: an indirect band gap with a value of 5.17–5.30 eV, and a direct band gap with a value of 5.75 eV. The indirect gap may be attributed to defect absorption, whereas the direct gap is related to fundamental absorption. Although there was a drastic change resulting from annealing the as-deposited films, in general, the properties of the films did not show significant changes upon annealing at temperatures in the range 400–800 °C. The annealed films were transparent and compact. Such characteristics make them favorable candidates for optical applications.

Acknowledgement

The support to this work by the Physics Department of King Fahd University of Petroleum and Minerals is acknowledged.

References

[1] M. Matsuoka, S. Isotani, S. Miyake, Y. Setsuhara, K. Ogala, N. Kuratani, J. Appl. Phys. 80 (1996) 1177.
[2] S. Venkataraj, O. Kappertz, H. Weis, R. Drese, R. Jayavel, M. Wuttig, J. Appl. Phys. 92 (2002) 3599.
[3] D.H. Kuo, C.H. Chien, C.H. Huang, Thin Solid Films 420–421 (2002) 47.
[4] W. Li, X. Liu, A. Huang, P.K. Chu, J. Phys. D: Appl. Phys. 40 (2007) 2293.
[5] S. Zhao, F. Ma, K.W. Xu, H.F. Liang, J. Alloys Compd. 453 (2008) 453.
[6] P.J. Martin, A. Bendavid, Thin Solid Films 518 (2010) 5078.
[7] Z.W. Zhao, B.K. Tay, L. Huang, G.Q. Yu, J. Phys. D: Appl. Phys. 37 (2004) 1701.
[8] R. Brenier, J. Mugnier, E. Mirica, Appl. Surf. Sci. 143 (1999) 85.
[9] W.-C. Liu, D. Wu, A.-D. Li, H.-Q. Ling, Y.-F. Tang, N.-B. Ming, Appl. Surf. Sci. 191 (2002) 181.
[10] G. Ehrhart, B. Capoen, O. Robbe, Ph. Boy, S. Turrell, M. Bouazaoui, Thin Solid Films 496 (2006) 227.
[11] S.-M. Chang, R. Doong, Chem. Mater. 19 (2007) 4804.
[12] R. Matero, M. Ritala, M. Leskela, A.C. Jones, P.A. Williams, J.F. Bickley, A. Steiner, T.J. Leedham, H.O. Davies, J. Non-Cryst. Solids 303 (2002) 24.
[13] Q. Guo, R.W. Joyner, Appl. Surf. Sci. 144–145 (1999) 375.
[14] R. Alvarez, A. Palmero, L.O. Prieto-Lopez, F. Yubero, J. Cotrino, W. de la Cruz, H. Rudolph, F.H.P. Habraken, A.R. Gonzalez-Elipe, J. Appl. Phys. 107 (2010) 054311.
[15] W.T. Tang, Z.F. Ying, Z.G. Hu, W.W. Li, J. Sun, N. Xu, J.D. Wu, Thin Solid Films 518 (2010) 5442.
[16] C. Flamini, A.G. Guidoni, R. Teghil, V. Marotta, Appl. Surf. Sci. 138–139 (1999) 344.
[17] J. Zhu, T.L. Li, B. Pan, L. Zhou, Z.G. Liu, J. Phys. D: Appl. Phys. 36 (2003) 389.
[18] J. Zhu, Z.G. Liu, Appl. Phys. A 78 (2004) 741.
[19] S.J. Wang, Y.F. Dong, C.H.A. Huan, Y.P. Feng, C.K. Ong, Mater. Sci. Eng. B 118 (2005) 122.
[20] J. Sellmann, Ch. Sturm, R. Schmidt-Grund, Ch. Czekalla, J. Lenzner, H. Hochmuth, B. Rheinlander, M. Lorenz, M. Grundmann, Phys. Status Solidi C 5 (2008) 1240.
[21] S.M. Edlou, A. Smajkiewicz, G.A. Al-Jumaily, Appl. Opt. 32 (1993) 5601.
[22] J.Q. He, A. Teren, C.L. Jia, P. Ehrhart, K. Urban, R. Waser, R.H. Wang, J. Cryst. Growth 262 (2004) 295.
[23] S.-M. Chang, R. Roong, Chem. Mater. 17 (2005) 4837.
[24] D.P. Norton, Mater. Sci. Eng. R: Rep. 43 (2004) 139.
[25] M.N. Ashfold, F. Claeyssens, G.M. Fuge, S.J. Henley, Chem. Soc. Rev. 33 (2004) 23.
[26] S. Zhao, F. Ma, Z. Song, K. Xu, Opt. Mater. 30 (2008) 910.
[27] O.S. Heavens, Optical Properties of Thin Solid Films, Dover, New York, 1991, p. 78.
[28] J.C. Manifacier, J. Gasiot, J.P. Fillard, J. Phys. E 9 (1976) 1002.
[29] S.H. Wemple, M. Didomenico, Phys. Rev. B 3 (1971) 1338.
[30] M. Ylilammi, T. Ranta-aho, Thin Solid Films 232 (1993) 56.
[31] I.H. Malitson, J. Opt. Soc. Am. 55 (1965) 1205.
[32] S. Venkataraj, O. Kappertz, Ch. Liesch, R. Detemple, R. Jayavel, Vacuum 75 (2004) 7.
[33] M. Harris, H. Macleod, S. Ogura, E. Pelletier, B. Vidal, Thin Solid Films 57 (1979) 173.
[34] P.J. Martin, R.P. Netterfield, T.J. Kinder, Thin Solid Films 193–194 (1990) 77.
[35] Y. Natsume, H. Sakata, Mater. Chem. Phys. 78 (2002) 170.
[36] B. Kralik, E.C. Chang, S.G. Louie, Phys. Rev. B 57 (1998) 7027.
[37] R.H. French, S.J. Glass, F.S. Ohuchi, Y.N. Xu, W.Y. Ching, Phys. Rev. B 49 (1994) 5133.
[38] M. Houssa, M. Tuominen, M. Naili, V. Afanas'ev, A. Stesmans, S. Haukka, M.M. Heyns, J. Appl. Phys. 87 (2000) 8615.
[39] M.-T. Wang, T.-H. Wang, J.Y. Lee, Microelectron. Reliab. 45 (2005) 969.